2021

Plasmaspheric dynamics studied using a three-dimensional machine learning-based plasma density model in the inner magnetosphere and the ionosphere

Hannah Ace
The University of Vermont

Recommended Citation

Ace, Hannah, "Plasmaspheric dynamics studied using a three-dimensional machine learning-based plasma density model in the inner magnetosphere and the ionosphere" (2021). *UVM Honors College Senior Theses*. 380.
https://scholarworks.uvm.edu/hcoltheses/380

Plasmaspheric dynamics studied using a three-dimensional machine learning-based plasma density model in the inner magnetosphere and the ionosphere

An Honors Thesis Presented
by
Hannah Ace
to
The Faculty of the University of Vermont
Spring 2021

Defense Date: 5th May, 2021
Thesis Examination Committee:

Bernard Cole, Ph.D., Chairperson
Xiangning Chu, Ph.D., Advisor
Valeri Kotov, Ph.D., Advisor
Juan Vanegas, Ph.D.

Abstract

Plasmaspheric density and composition strongly influence wave growth and propagation, as well as energetic particle scattering. Previous statistical, empirical plasma density models of the inner magnetosphere have limited capability to make accurate predictions. Consequently, these models cannot be used to adequately quantify complex global processes and nonlinear responses to driving conditions, factors of critical importance during geomagnetic storms. Recent advancements in machine learning techniques have enabled a more dynamic study of the space environment. Here we present two three-dimensional dynamic electron density models (one magnetospheric model and one ionospheric model) based on an artificial neural network. The models use feedforward neural networks which were generated using electron densities from satellite missions of CRRES, ISEE, IMAGE, POLAR, and DMSP. The three-dimensional electron density model takes spacecraft location and time series solar wind conditions (e.g., flow speed, plasma density, solar radiance) and geomagnetic indices (e.g., AP index, AE and AL indices, F10.7 index, Dst index, KP index, PCN index, and solar Lyman-Alpha flux) obtained from NASA's OMNI database as inputs. When compared with the out-of-sample data, the three-dimensional models predict equatorial and field-aligned density profiles from satellite measurements with root mean square errors of 0.410 and 0.622, respectively. When the three-dimensional magnetospheric model is applied to a geomagnetic storm, successful reconstruction of the expected plasmaspheric dynamics, such as the plasmaspheric erosion, and plume formation in three dimensions was achieved.

Acknowledgements

I want to thank my research mentor Xiangning Chu, for all of the mentorship, guidance, and constant help, without which this would not have been possible, and my advisor Valeri Kotov for helping me to navigate the thesis process. I also want to thank all of my professors from UVM, in particular John Perry for first sparking my love for astronomy and being a constant source of guidance and support ever since.

This work used the Extreme Science and Engineering Discovery Environment (XSEDE) Bridges GPU at the PSC through allocation TG-PHY190033, which is supported by National Science Foundation grant number ACI-1548562.

I also want to thank the NSF funding of the Boulder Solar Alliance REU program for supporting this research.

Table of Contents

Introduction

1.1 Plasmaspheric Composition and Dynamics

The difference in gas pressure between the solar corona and interstellar space results in a flow of ionized solar plasma and remnants of the solar magnetic field to be driven outward and away from the sun. This solar wind is comprised mainly of ionized hydrogen (or protons and electrons in equal numbers), along with a smaller percentage of ionized helium and heavier elements [*Kivelson and Russell*, 1995]. Where the solar wind meets the magnetic field of the Earth , the pressure of the solar wind and the Earth's magnetic field, which also contains plasma, establish an equilibrium. Thus, a bubble of sorts forms around the Earth, which is referred to as Earth's magnetosphere. The magnetosphere is usually divided into three regions: the ionosphere, the plasmasphere or inner magnetosphere, and the outer magnetosphere. The magnetosphere also contains charged particles that interact with the remnants of the solar magnetic field contained within the solar wind.

Earth's magnetospheric environment is comprised of several components including, as described by *Bortnik et al.* [2016], "the ionosphere, background electric and magnetic fields, plasma waves, electrons ranging from cool (1 eV) to ultrarelativistic (> 5 MeV) energies, and different species and energies of ions." All these components have both external driving factors, such as the solar wind, and internal driving factors including various other instabilities. In addition to this, they often couple to one another in complex and nonlinear ways that are not easy to predict via simple mathematical models [*Bortnik et al.,* 2016]. This fact results in a dynamic environment that cannot be sufficiently empirically modeled through the use of statistical models.

The plasmasphere is a region in Earth's inner magnetosphere, between the upper atmosphere and the plasmapause, containing cold and dense plasma. [*Carpenter*, 1966; *Nishida*, 1966*; Lemaire et al*., 1998; *Darrouzet et al.*, 2009]. This system in Earth's inner magnetosphere is inextricably connected to the Sun and is driven by energy inputs from the solar wind [*Bortnik et al.,* 2016]. During quiet times, when there is minimal geomagnetic activity, the charged particles in the plasmasphere exist in dynamic equilibrium with the upper ionosphere. When a disturbance occurs, such as during a geomagnetic storm, the enhanced magnetospheric convection causes an erosion of the plasmasphere to lower L shells—in other words, the plasmasphere erodes radially, as seen in the satellite image in Figure 1 [*Chu et al.,* 2017a, b]. Simultaneously, the afternoon region of the magnetosphere is drawn towards the dayside magnetopause, and a Plasmaspheric plume forms as a result [*Grebowsky,* 1970; *Ober et al.,* 1997; *Goldstein et al.,* 2004; *Darrouzet et al.,* 2008]. This convection is followed by a period of storm-time recovery, wherein the low-energy ionospheric plasma is pulled from low latitudes upward along the magnetic field lines, and previously emptied regions are refilled. This dynamic cycle constantly repeats, with the erosion influenced by geomagnetic activity occurring on the order of a few hours and the subsequent refilling occurring over a few days *[Kersley and Klobuchar,* 1980; *Dent et al.,* 2006; *Sandel and Denton,* 2007; *Foster et al.,* 2014].

The electrically charged particles found in the ionosphere are ionized by extraterrestrial radiation, affecting the propagation of radio waves [*Li et al.,* 2021]. Thus, plasmaspheric density and composition strongly influence wave growth and propagation, as well as energetic particle scattering [*Chu et al.,* 2017a, b]. In addition to this, low energy electrons in the plasmasphere significantly influence the acceleration of relativistic electrons with high speeds and high energies. Such "killer" electrons can affect both satellites and astronauts and are therefore of key interest in the study of space weather. Previous empirical models are independent of time and geomagnetic activity [*Sheeley et al*., 2001], and thus fail to accurately describe the electron density at any time or region. Therefore, the development of machine learning models is necessary to quantify effects on the plasmasphere due to geomagnetic storms, and to fully understand Plasmaspheric dynamics and space weather.

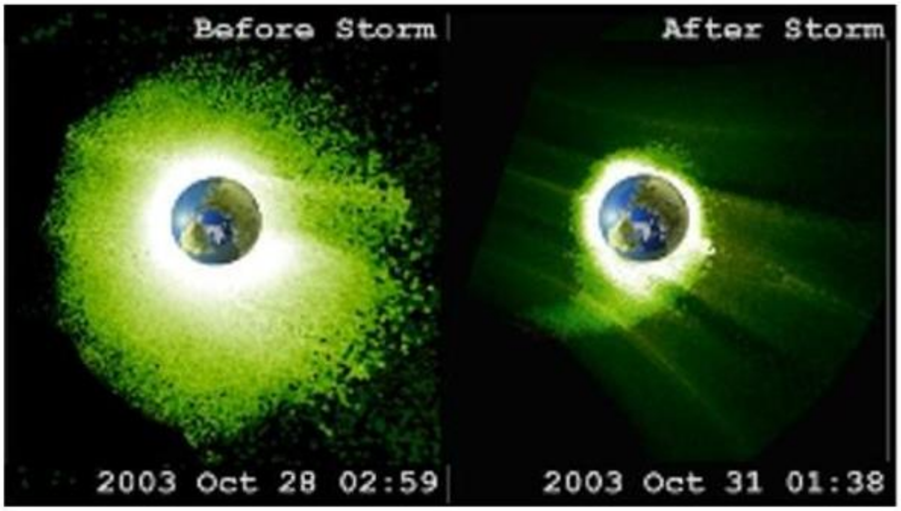

Figure 1: (2005: Goldstein et al.) Satellite observations show the contraction of the plasmapause due to geomagnetic storms.

1.2 Previous Work and Significance

Plasma density, or equivalently electron density number, in the equatorial plane and along magnetic field lines has been modeled statistically in the past via several empirical models [*Carpenter and Anderson*, 1992; *Sheeley et al.*, 2001; *Gallagher et al.*, 2000; *Denton et al.*, 2002a, 2002b, 2004; *Tu et al.*, 2006; *Reinischet al.*, 2009; *Ozhogin et al.*, 2012]. The equatorial plasma density is usually modeled with two empirical functions for trough and plasmaspheric densities, expressed either as exponential or power-law functions, or some mix of the two, and a function for plasmapause location [*Carpenter and Anderson*, 1992; *Sheeley et al.*, 2001]. The following model by *Carpenter and Anderson* [1992] was developed using observations from the satellite ISEE. The Plasmaspheric density is given by the following function:

$$log_{10}n_e = (-0.3145L + 3.9043) + [0.15(\cos\frac{2\pi(d+9)}{365}) - 0.5\cos\frac{4\pi(d+9)}{365}) + 0.00127\bar{R} - 0.0635]e^{\frac{-L-2}{1.5}}$$

where d is the number of days representing seasonal variations and $\bar{R}$ is the 13 month-average sunspot number. Here, L refers to the L shell, which describes the magnetic field line that crosses the magnetic equator at a number of Earth-radii equal to the L-value. Together with magnetic local time (MLT) and magnetic latitude (MLAT), it makes up a coordinate system somewhat similar to r, θ, and φ in spherical coordinates. MLAT is a coordinate similar to the geographic latitude, except it is defined relative to the geomagnetic poles rather than the geographic poles. MLT can be defined as the hour angle from the midnight magnetic meridian, increasing positively in the magnetic eastward direction. The midnight magnetic meridian is defined as the meridian 180º in magnetic longitude away from the subsolar point. Therefore, the MLT/MLAT coordinate system rotates with respect to Earth at the same rate that the subsolar point crosses magnetic meridians [*Laundal et al.,* 2016].

The trough density is given by the following function which depends on MLT:

$$n_e = (5800 + 3000MLT)L^{-4.5} + \left(1 - e^{\frac{-L-2}{10}}\right), 00 \leq MLT \leq 06$$

$$n_e = (-800 + 1400MLT)L^{-4.5} + \left(1 - e^{\frac{-L-2}{10}}\right), 06 \leq MLT \leq 15$$

The plasmapause location is given by:

$$L_{pp} = 5.6 - 0.46Kp_{max}$$

where Kp_{max} is the maximum value of Kp in the previous 24 hours.

The functions for electron density in the trough and plasmasphere were later developed with the addition of observations from the satellite CRRES, which covers a larger range of MLT values [*Sheeley et al.,* 2001]. The updated function for the plasmaspheric density is given by:

$$n_e = 1390\left(\frac{3}{L}\right)^{4.83}, 3 \leq L \leq 7$$

and the updated function for the trough density is:

$$n_e = 124\left(\frac{3}{L}\right)^{4.0} + 36\left(\frac{3}{L}\right)^{3.5} \cos\left(\frac{\left\{LT - \left[7.7\left(\frac{3}{L}\right)^{2.0} + 12\right]\right\}\pi}{12}\right), 3 \leq L \leq 7$$

As seen in the preceding equations of the Carpenter and Anderson model, the electron densities in the Plasmaspheric and trough regions are a function of L shell and magnetic local time (MLT) and are thus independent of both time and geomagnetic activity [*Sheeley* et al., 2001]. Additionally, the function for the plasmaspheric density considers the solar cycle effects only by the 13 month-average of sunspot number and by the day number, which consider semiannual variation. Therefore, the equation for plasmaspheric density is only weakly dependent on the long-term effects of the solar cycle, as well as the seasonal effect [*Carpenter and Anderson,* 1992].

The field-aligned distribution of the plasma density has also been examined using various data sets and methods. The global core plasma model (GCPM) [*Gallagher et al.,* 2000] uses an exponential function to interpolate between the topside ionospheric profile of the International Reference Ionosphere model and the equatorial Plasmaspheric density profiles [*Gallagher et al.,* 2000] in order to obtain the field-aligned density profile. In situ observations made by the plasma-wave instrument aboard the Polar satellite were later used to study field-aligned distributions [*Goldstein et al.,* 2001; *Denton et al.,* 2002a, 2002b]. Here, the field-aligned plasma density was modeled using a power-law as follows:

$$n_e = n_{e0}\left(\frac{LR_E}{R}\right)^{\alpha} = n_{eO}\, sec\, \lambda^{2\alpha}$$

Where n_{e0} is the electron density at the equator, L is the L shell, R_E is the radius of the Earth, R is the geocentric distance from the Earth's center, λ is the magnetic latitude (MLAT), and α is a function of L shell. The parameter of α was fitted under an assumption of no MLT or temporal variations, defined as when a polar-orbiting satellite crossed the same L shell. In addition to in situ measurements, the field-aligned distribution was constructed using echo observations from the radio plasma imager aboard to IMAGE satellite [*Reinisch et al*., 2001; *Huang et al*., 2004; *Tu et al.,* 2006; *Ozhogin et al.,* 2012]. The field-aligned density was also sometimes obtained simultaneously in both hemispheres, in this case being expressed in a more compact form:

$$n_e = n_{e0}\, cos^{-\beta}\left(\frac{\Pi}{2}\frac{\alpha\lambda}{\lambda_{inv}}\right)$$

where n_{e0} is again the equatorial electron density, λ is the magnetic latitude, and λ_{inv} is the magnetic invariant latitude. The parameters α and β control the flatness and steepness of the field-aligned density profiles and were fitted based on specific events [*Huang et al*., 2004; *Reinisch et al.,* 2004] and statistically [*Ozhogin et al.,* 2012].

Most empirical models are expressed as functions of L shell and have no dependence on geomagnetic activity or time, and furthermore fail to take into account the effects on charged particles of the magnetosphere from several solar-terrestrial factors, including solar flux, geomagnetic storms, neutral winds, and the electric field [*Anderson et al.,* 1998; *Atıcı & Sağır,* 2020; *Du et al.,* 2019; *Karatay,* 2020; *Schunk et al.*, 1975]. A time-dependent model of the inner magnetosphere's electron density, however, is very important for a variety of applications. For example, by using in-situ observations of electron density obtained by the Van Allen probes (rather than a statistically averaged empirical model) a much better comparison between modeled and observed electron acceleration during a major radiation belt enhancement on October 8th-9th of 2012 was drawn [*Thorne et al.*, 2013]. Unfortunately, satellite observations of electron densities are not available for every storm event, so this is not a practical approach to modeling plasmaspheric dynamics. In addition to this, it is not the in situ density but rather the global distribution of the electron density which is required for modeling wave-particle interactions. This is because electron acceleration occurs over extended paths along an electrons' drift orbit, not simply where in situ density measurements are obtained [*Chu et al.,* 2017]. A time and geomagnetic activity-dependent and global model of the electron density is therefore essential to understand wave growth propagation and particle scattering. In addition to this, cold electrons in the plasmasphere significantly influence the acceleration of relativistic electrons with high speeds and high energies. Such "killer" electrons can affect both satellites and astronauts and are therefore of key interest in the study of space weather.

In order to model the dynamic evolution of the plasmasphere due to storm-induced erosion and refilling, a time-dependent equatorial plasma density model has been developed by *Bortnik et al.* [2016] and *Chu et al.* [2017a, b] using a neural network approach with time series of solar and geomagnetic indices as inputs. This neural network model has successfully reconstructed dynamic behaviors and density features, including quiet time plasmasphere, erosion, recovery, and plume formation during storm events.

1.3 Machine Learning and Neural Networks

Recent advancements in machine learning techniques have enabled a more dynamic study of the space environment. Artificial neural networks (ANN) are useful in representing complicated functions such as the complex, nonlinear dependence of electron density dynamics.

The structure of neural networks is inspired by the brain: a network is comprised of neurons, which make up layers. Each neuron contains an activation which determines the activation in the following layers. In addition, the connections between neurons have weight assigned to them, which are multiplied by all of the activations in the layer to give the weighted sum of that layer. At the input layer, the neural network is given a set of training data, and the weights and activations are initially randomized. The weighted sum at that layer is then computed by the following equation:

$$z = f\sum_{i}(a_i w_i + b_i)$$

where i denotes the layer, a is the activation, w is the associated weight, and b is the bias. The entire weighted sum is wrapped in an activation function, f, such as the sigmoid function. This function condenses the values onto a number line between 0 and 1 so that very negative values are close to zero and very positive ones are close to one. The bias is added so that the neuron only lights up when the weighted sum is larger than some non-zero number. The learning process is finding valid values for all the weights, activations, and biases to accurately solve the problem. At the final output layer, a cost function is defined to tell how accurate the output is. By adding the squares of the differences between each output activation and the desired output, provided by a validation data set which is held out of the training processes, the accuracy of the output can be determined. The goal is then to find the minimum of the cost function, which is often very complex. This can be done by starting at any random input and determining which direction it must move to lower the cost. This is done repeatedly until a local minimum is found. Since there may be many local minima, strategies such as early stopping are used to help find the correct minimum. Through this process the model can be trained to minimize the cost and produce the most accurate output.

Database

2.1 Overview

In this study, two DEN3D dynamic electron density models were developed using in situ electron density observations from the instruments aboard eight satellites. The first model focuses on the magnetosphere covering $2<L<6$, using in-situ measurements from four satellites CRRES, IMAGE, ISEE, and POLAR. The second model focuses on the ionosphere covering an altitude of ~850 km, using in-situ density data from four DMSP satellites. The input parameters for the two models include the position of the measurements and the geomagnetic activity indices. The position parameters are given in MLT, MLAT, and L shell coordinates for the magnetospheric model, and altitude, MLT, and MLAT for the ionospheric model. The geomagnetic indices include the solar wind conditions (e.g., flow speed, plasma density, solar radiance) and geomagnetic indices (e.g., AP index, AE and AL indices, $F_{10.7}$ index, Dst index, KP index, PC_N index, and solar Lyman-Alpha flux). A description of the various geomagnetic indices follows.

2.2 OMNI

The geomagnetic parameters which describe the solar wind are all are obtained from the OMNI database of NASA's Space Physics Data Facility. The Dst index is a measure of magnetic activity derived from a series of equatorial geomagnetic observations which measure the intensity of the globally symmetrical equatorial electrojet, or "ring current" [*Center, National Geophysical Data*, 2010]. SYM-H index dictates the intensity of magnetic storms. It is similar to the DST index, but with a much higher time-resolution [*Cai et al.,* 2009]. Both Dst and SYM-H indices are designed to measure the intensity of the storm time ring current. While Dst has a 1-hour time resolution, SYM-H has a 1-min time resolution. [*Wanliss et al.*, 2006]. AE index provides a global measure of the auroral zone magnetic activity caused by increased Ionospheric currents flowing below and within the auroral oval [*Center, National Geophysical Data*, 2010]. As stated by *Kamide et al.*, it is defined by "the separation between the upper and lower envelopes of the superposed H component plots from auroral-zone magnetic observatories”. Thus the relationship is given by AE = AU – AL, where AU and AL indices are the upper and lower envelopes, respectively [2004]. The AE index (and therefore the AL and AU indices) describe the disturbance level recorded by auroral zone magnetometers and the AL index monitors the strength of the westward electrojet [*McPherron et al.*, 2015]. The AP index is another measure of geomagnetic disturbance uniquely associated with storm events [*Fu et al.*, 2010]. The $F_{10.7}$ index is spot measurements of the solar radio flux density at 10.7 cm wavelength and is an indicator of solar activity [*Tapping et al.*, 1994]. It coordinates well with the sunspot number and a number of ultraviolet and visible solar irradiance records [*Center, National Geophysical Data*, 2010]. The KP index is an indicator of disturbances in the Earth’s magnetic field and is a measure of the strength of the solar-wind flux [*Dessler et al.*, 1963]. The PC_N index is a measure of the magnetic activity at the northern polar cap generated by the solar wind and the magnetic field [*Troshichey et al.,* 2006]. The solar Lyman-alpha flux is useful to examine and model solar and solar irradiance processes [*Machol et al.,* 2019].

2.3 CRRES, IMAGE, ISEE, POLAR

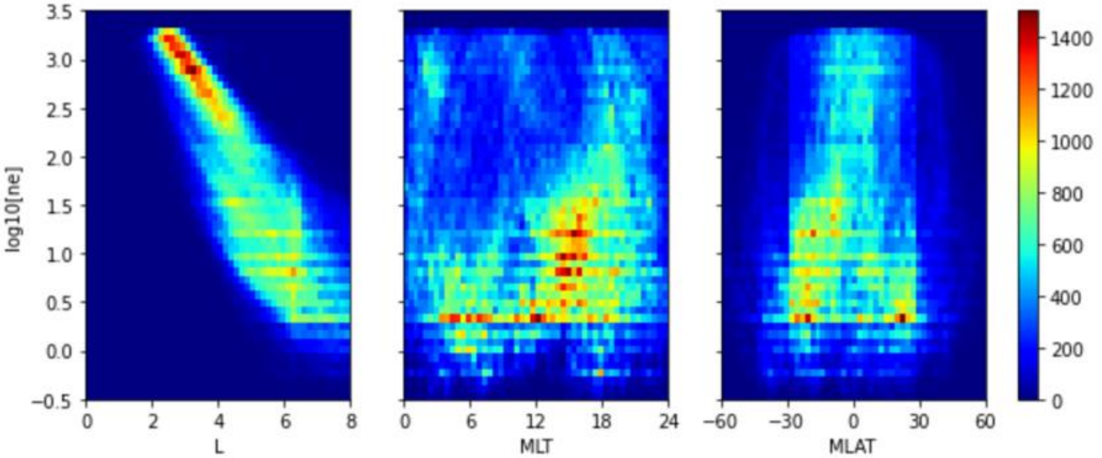

Figure 2: Distributions of in situ electron density observations, $\log_{10}(n_e)$, with respect to (in order from left to right) L shell (between 1 and 8), MLAT (between -60 degrees and 60 degrees), and MLT (between 0 hours and 24 hours). The bin sizes are 50 for L shell, MLAT, MLT, and electron density, and the colorbar shows the number of observations in each bin.

For the magnetospheric density model the in-situ electron density was obtained using the upper hybrid resonance frequency, or plasma frequency, identified from the continuum edge from the instruments on board four satellites [Chu et al., 2017a, b]. These four instruments include the plasma wave experiment onboard ISEE, which ran from October 27th 1977 to September 25th 1987 [Gurnett et al., 1978], the plasma wave experiment onboard CRRES, which ran from August 1st 1990 to October 13th 1991 [Anderson et al., 1992], the plasma wave experiment onboard Polar, which ran from March 26th 1996 to September 17th 1997 [Gurnett et al., 1995], and the radio plasma imager (RPI) onboard IMAGE, which ran from January 1st 2001, to December 19th 2005 [Reinisch et al., 2000]. The temporal resolution of the data was interpolated to a 5-minute resolution to save computational time. The relative error of the electron density derived from the wave measurements typically is less than 20% [Reinisch et al., 2004], varying slightly based on the frequency resolution of the wave instrument.

Figure 2 show the two-dimensional histograms of the electron density measurements $\log_{10}(n_e)$ versus L shell, MLAT, and MLT. The log of the electron density, $\log_{10}(n_e)$ versus the L shell is shown on the left. The greatest concentration of measurements is at L shells of between 1.5 to 4, and the distribution of the electron density decreases linearly with respect to the L shell. This is expected based on the power-law and exponential functions presented in the previous empirical models of *Carpenter and Anderson* [1992] and *Sheeley et al.* [2001]. At higher L shells, the density decreases. These higher L shell regions usually corresponds with the trough region of the plasmasphere, where the distribution of electrons is more spread [Che et al., 2017]. In the magnetospheric density model, we focus on the inner magnetospheric region and thus limit the data to observations within L shell 8. The center plot in Figure 2 shows $\log_{10}(n_e)$ versus MLAT, centered around the equator and restricted to $-60^o < \text{MLAT} < 60^o$. The rightmost plot in Figure 2 shows $\log_{10}(n_e)$ versus MLT. The electron densities cover all MLTs between 0 and 24 hours. The number of measurements of densities $\log_{10}(n_e) > 2$ is more uniform, while the number of observations of densities $\log_{10}(n_e) < 2$ is slightly higher in the afternoon region (12 and 18 MLT) due to the orbits of the satellite.

2.4 DMSP

In the ionospheric model, the electron densities were obtained using data from The Defense Meteorological Satellite Program (DMSP), which is comprised of satellites in Sun-synchronous polar orbits near 850 km altitude with orbital periods of around 104 minutes [*Fu et al.*, 2010]. Figure 3 shows the known orbit of the satellites DMSP-15, DMSP-16, DMSP-17, and

DMSP-18. From Figure 3, it can be seen that satellite 15 orbits between about 15 and 4 hours in MLT, satellite 16 orbits between about 16 and 5 hours in MLT, satellite 17 orbits around about 18 and 6 hours in MLT, and satellite 18 orbits between about 20 and 8 hours in MLT.

Figure 4 shows the number of in situ electron density measurements versus altitude, MLAT, and MLT, respectively for all four DMSP satellites. The leftmost plot shows $\log_{10}(n_e)$ vs. the altitude. The number of measurements is greatest around 850 km, since all four satellites orbit near 850 km altitude. In the plot of MLT versus electron density, the measurements are centered around MLTs of 4-8 hours on the low end and 15-20 hours on the high end. In the rightmost plot of MLAT versus electron density, the measurements are seen between latitudes of -90º (south pole) and 90º (north pole), which is the range of latitudes covered by the satellites.

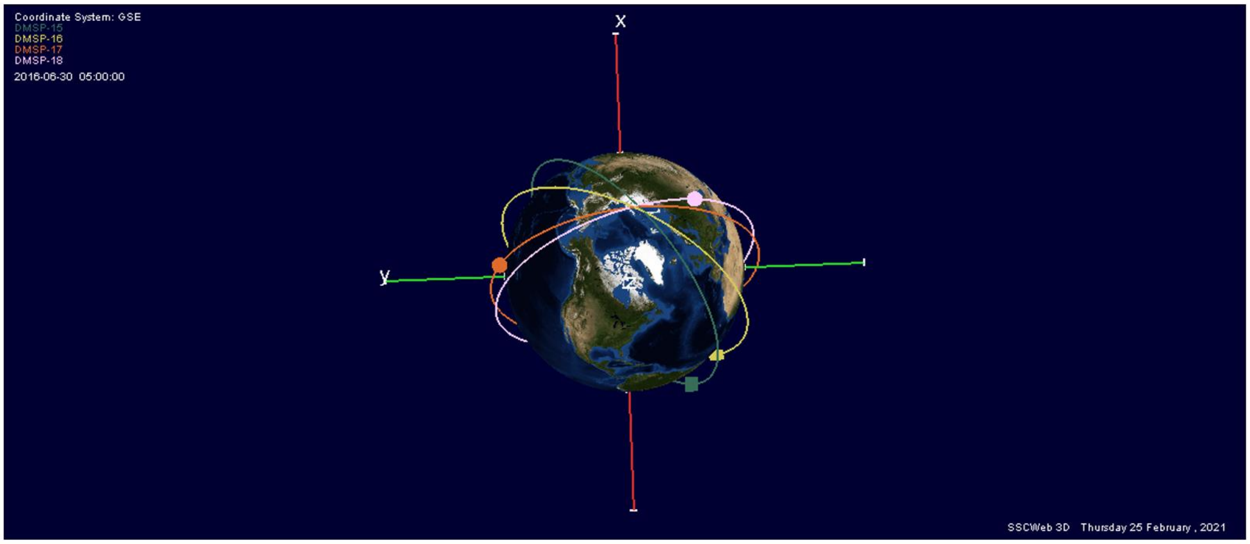

Figure 3: 3-dimensional rendering of the orbits of the four satellites DMSP-15 (shown in green), DMSP-16 (shown in yellow), DMSP-17 (shown orange), DMSP-18 (shown in pink). The figure is produced using SSC 4D orbit viewer available at https://sscweb.gsfc.nasa.gov/tipsod/

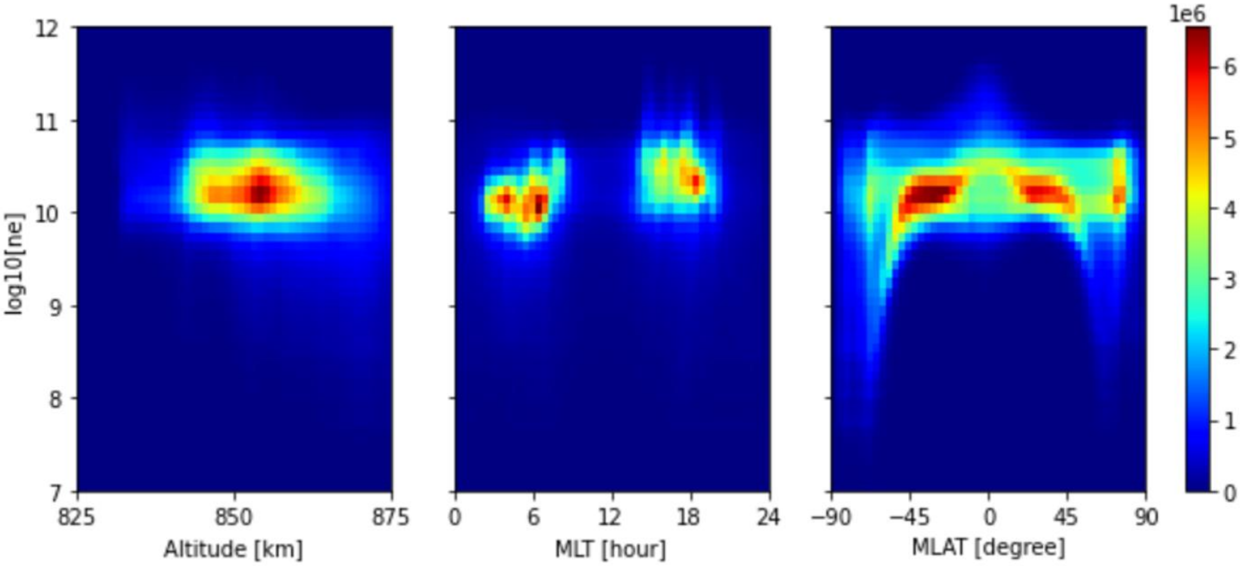

Figure 4: Distributions of in situ electron density observations, $log_{10}(n_e)$, with respect to (in order from left to right) altitude (between 825 km and 875 km), MLT (between 0 hours and 24 hours), and MLAT (between -90 degrees and 90 degrees). The bin sizes are 50 for L shell, MLAT, MLT, and electron density, and the colorbar shows the number of observations in each bin.

Methodology

3.1 Procedures

The first step in building the model involved data processing. The electron density and positional data from all eight satellites were first read and then plotted over all time steps in order to check for abnormalities which needed to be removed. For example, when processing the CRRES, IMAGE, ISEE, and POLAR data, any data corresponding to L shells of 0 or MLT's greater than 24 were removed because they did not reflect what was expected of the data physically and were therefore identified as anomalies. After all the data had been checked for abnormalities, the ensembles could be created for use in the model training.

XSEDE is a virtual system that can be used to share computing resources and data. Through XSEDE, the Pittsburg Supercomputing Center was used to process data for the ionospheric model. In addition to this, Google Colab was used to process the data for the magnetospheric model. When creating the ensembles for the first model (using CRRES, IMAGE, ISEE, and POLAR data) the positional, electron density, and OMNI data, were all first interpolated in order to fill large gaps in the data where no satellite observations were available. The OMNI data was then interpolated onto the timestamps of the satellite data, because the OMNI data is much lower resolution than the CRRES, IMAGE, ISEE, and POLAR data, and thus the ensemble dimensions over the same time steps did not match. In total, each input (electron density, position, and time) of the CRRES, IMAGE, ISEE, and POLAR data had 2,609,661 points when interpolated. An array was created of interpolated OMNI data at several different shifted time steps in order to have a temporally larger range of geomagnetic indices. Two arrays were then created, one with the interpolated positional data and the various time shifts of the interpolated OMNI data, and one of the interpolated electron density data. All non-finite numbers were then removed from the data. The input and target parameters were then normalized by calculating the standard deviation and mean of each ensemble, and then calculating a new set which was the original ensemble minus the mean and divided by the standard deviation. The data was then split into random training and test datasets via the sklearn.model_selection.train_test_split module, which takes an array as an input and randomly splits the data into sets for training and testing along with a given percentage. For this model, the training size was set to 70% of the data, and the test size was set to 30% of the data. The model was then defined by setting the number of neurons in each hidden layer as well as the activation function and loss, which are described in more detail in the ‘Model Architecture’ section. The model was then trained using the TensorFlow and Keras libraries, including callbacks such as early stopping to improve model generability. When the root mean square error is minimized, the training stops, and the model performance can be evaluated. The performance was then evaluated using the root mean square error to calculate the error factor, and by plotting the model’s predicted electron density, and comparing it to the observed electron density which was held out of the model. Once the model achieved a satisfiable level of performance, it was applied to a geomagnetic storm event to examine the predictive abilities further. In order to do this, a virtual grid of L shell versus MLT was created on which to project electron density predictions. The magnetospheric model was then used to predict the electron density at four-time steps during the storm event, and the predictions were plotted onto the virtual grid in order to search for recognizable features of the plasma density evolution.

This process was then repeated for the model trained using the DMSP data. For this model, after the data was processed, slightly less than 7% of the DMSP data was randomly selected for use in the training using numpy.random.permutation, because of the huge size of the DMSP data. In total, each input (electron density, position, and time) of the DMSP data from each satellite had 336,089,655 points. In the model training, only 20,000,000 of those points were used. The OMNI data were then interpolated onto the timestamps of the DMSP data. The same processes as described above were then used for the creation of the ensembles and training. The geomagnetic event reconstruction was attempted but was ultimately unsuccessful, as described further in the Results and Application section of this paper.

3.2 Model Architecture

Traditional neural networks contain an input layer, several hidden layers, and an output layer. Each layer contains multiple neurons. The output of each neuron is used as the input of the following node via their associated weight, and the output of each neuron within the hidden layers is computed using an activation function such as Tansig, sigmoid, Relu, or Tanh [Li et al., 2021]. In the model used for this study, the sigmoid was used as the activation function. During the training process, the neural network updates the weights and biases based on the mean square error calculated at the output layer, and the training stops when that mean square error is minimized. The architecture of the ANN model is shown in Figure 5, with 30 and 10 neurons respectively in the first and second layers. The model is similar to those developed in previous studies by *Bortnik et al.* [2016] and *Chu et al.* [2017a, b], both of which successfully model the equatorial plasma density global dynamic distributions. The input of each neuron, given by $z_j^l = f\left(\sum_{i=0}^{N-1} w_{ij} + b_j\right)$, is a product of the output of the previous node and its associated weight, where i and j are the neuron number in the current and preceding layers, respectively, and wij and bi are the weights and biases in the hidden layer. The sigmoid activation function, which calculates the output of each neuron, is given by $f(z^l) = 1 / (1 + exp(-z^l))$ [*Chu et al.*, 2017a]. The DEN3D model is trained using backpropagation to minimize the mean square error (MSE) of log10(ne). A randomly chosen portion of the database totaling 70% of the database is used as the training set, and 30% is held out as the validation set. The training set is the set of data used to fit the parameters, such as the weights of the connections between neurons, during the training process. The training set is usually made up of input vectors and the corresponding output vectors [*Li et al.*, 2021]. In this case the training set consisted of the positional data and various solar wind parameters (as input vectors) and the log of the electron density (as output vectors). The validation set is held out of the model and is used to evaluate the model's performance. The training process stops updating weights and biases when the cost of the validation set stops improving for several consecutive steps [*Chu et al.*, 2017a]. These early stopping criteria are useful to avoid overfitting of the model and improve the generalizability of the DEN3D model.

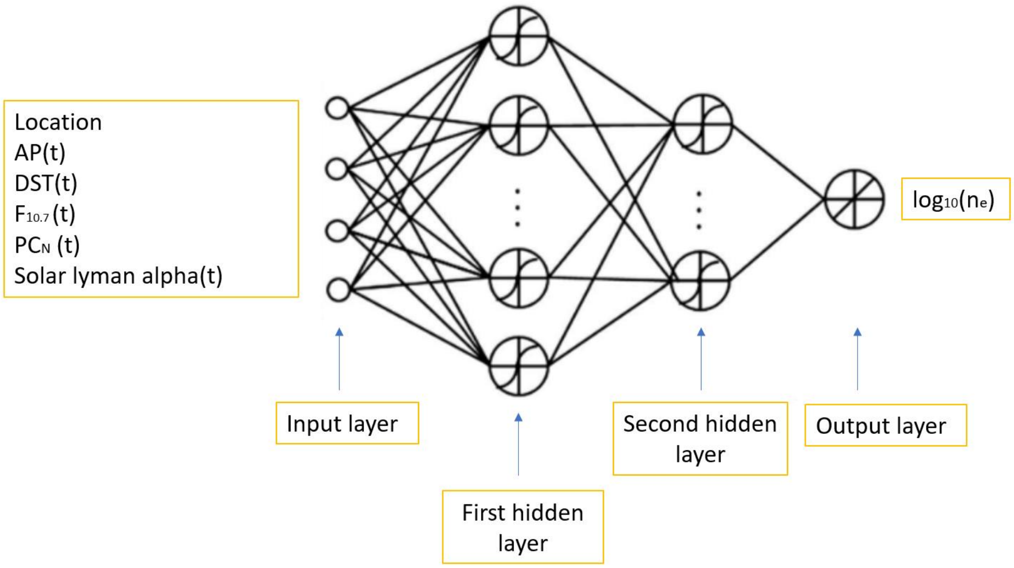

Figure 5: The ANN model has 30 and 10 neurons in the first and second hidden layers, respectively. The input parameters for the model using the DMSP data include location data of the measurements (Altitude, MLT, and MLAT), geomagnetic indices (AP, DST, PCN, Solar lyman alpha), and solar EUV index (F10.7). The target of the model is the log of the electron density, log10(ne)

Results and Application

4.1 Model Performance

Figure 6 shows the comparison between the observation and model prediction for a randomly selected data set data for the magnetospheric density model. The plot shows the model's predictions versus the validation data for 50 random data points. The validation data, which was held out of the model, is shown in blue. The model's prediction is shown in red. From Figure 6, it can be seen that there is very good agreement between the observed data and the model's prediction. Figure 7 shows the two-dimensional histogram between the observed and modeled electron density for the magnetospheric density model. The colorbar shows the number of observations in each bin, and the light blue diagonal line represents perfect agreement between the model's prediction and observations (y = x). Most of the data points are clustered around the diagonal, indicating that most of the observations can be modeled accurately. The root mean square error (RMSE) of the test data set of $\log_{10}(n_e)$ is 0.410, giving an error factor of $10^{0.410} = 2.57$. The RMSE is calculated by subtracting the log of the predicted electron density from the log of the observed electron density according to the following equation:

$$\log(n_{e,observed}) - \log\left(n_{e,modeled}\right) = \pm\mathrm{RMSE}$$

thus it can be found that

$$\log\left(\frac{n_{e,observed}}{n_{e,modeled}}\right) = \pm\mathrm{RMSE}$$

$$\frac{n_{e,observed}}{n_{e,modeled}} = 10^{\pm\mathrm{RMSE}}$$

Here, the RMSE is 0.410, so $\frac{n_{e,observed}}{n_{e,modeled}}$ has a value of $10^{\pm 0.410} = 2.57$ or 0.389. In other words, $n_{e,observed} = 2.57 * n_{e,modeled}$ or $n_{e,observed} = 0.389 * n_{e,modeled}$. Therefore, if the predicted density is 1.0 g/cm^3, the modeled density has a standard deviation between 0.389 and

2.57. This is close to the intrinsic uncertainty level of the instrument measurements of the plasma density, which is a factor of 2 [*Chu et al.*, 2017a]. This means that this DEN3D model has the ability to predict out-of-sample observations with uncertainty between a factor of 2 and 3.

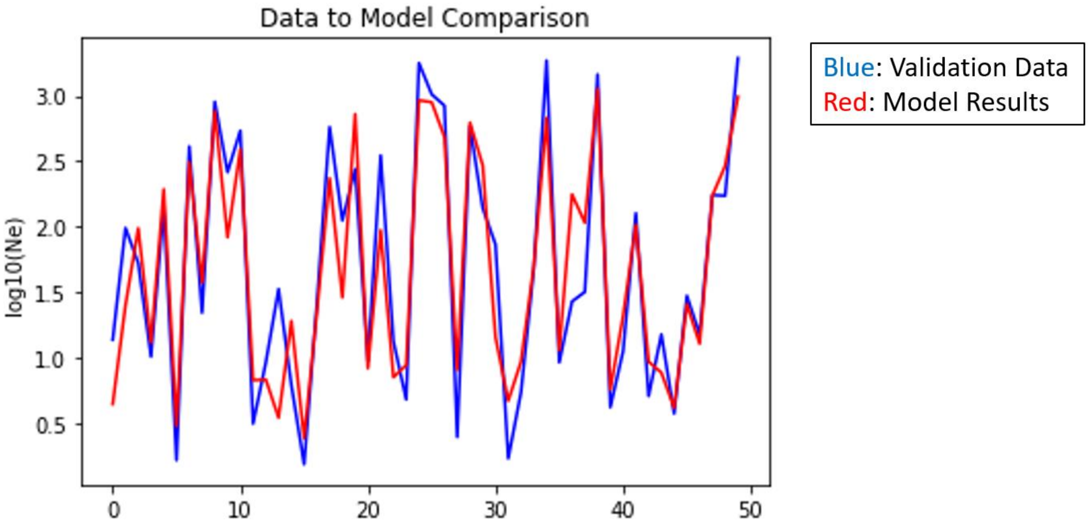

Figure 6: The data to model comparison for a randomly selected set of 50 data points of the model trained using CRRES, IMAGE, ISEE, and POLAR data. The validation data, which was held out of the model , is shown in blue. The model's predicted results are shown in red.

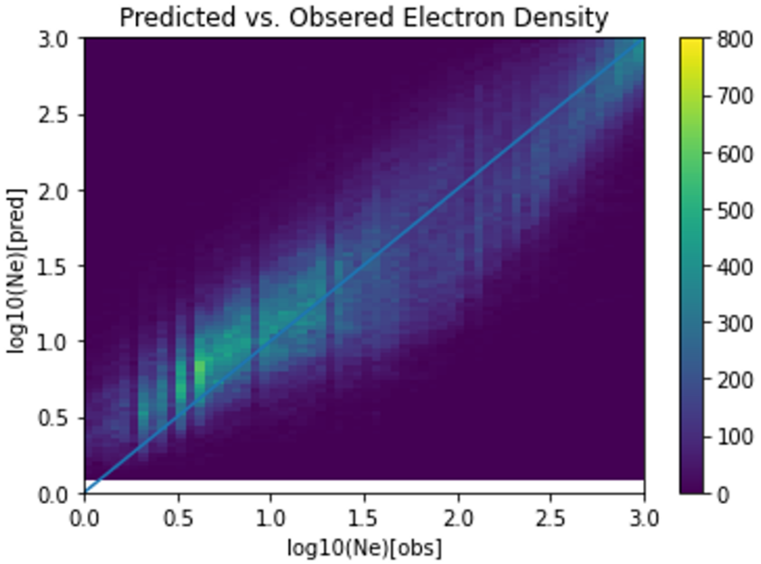

Figure 7: The correlation between the observed electron density and the model's predication of the electron density for the model trained using the CRRES, IMAGE, ISEE, and POLAR data. The bin size for both the observed and predicted density is equal to 100. The color bar shows the number of observations in each bin. The light blue diagonal line given by y = x indicates perfect agreement between the model's predictions and observed data.

In Figure 8 the data to model comparison for the model trained using DMSP data is shown for a randomly selected set of data. The plot shows the model's predictions versus the validation data for 50 random data points. The validation data is again shown in blue, while the model's prediction is shown in red. The plot shows good agreement between the observed data and the model's prediction, although not as good as the model trained using the CRRES, IMAGE, ISEE, and POLAR data. In Figure 9 the correlation between the observed electron density and the model's prediction of the electron density is shown. The colorbar shows the number of observations in each bin, and the red diagonal line at y=x represents perfect agreement between the model's prediction and observations. From this plot, we can again assume that most of the observations can be modeled accurately. The root mean square error (RMSE) of the test data set of log10(ne) is 0.622 giving an error factor of $10^{0.622} = 4.19$. This means that the DEN3D model has the ability to predict out-of-sample observations with an error within a factor of 5. The error of the ionospheric model using DMSP data is higher than the error of the magnetospheric model using CRRES, IMAGE, ISEE, and POLAR data is because the DMSP model is trained using instantaneous input parameters, while the model using CRRES, IMAGE, ISEE, and POLAR data is trained using a time series of input parameters. Time series indices are the preferred input over instantaneous values because the plasmaspheric and ionospheric state varies strongly depending on its current state and preceding states. However, a time series of input parameters were not used in the DMSP model because of the large data size. Therefore, it is expected that the DMSP model has a lower performance than the magnetospheric model.

Figure 8: The data to model comparison for a randomly selected set of 50 data points from the model trained using DMSP data. The validation data, which was held out of the model , is shown in blue. The model's predicted results are shown in red.

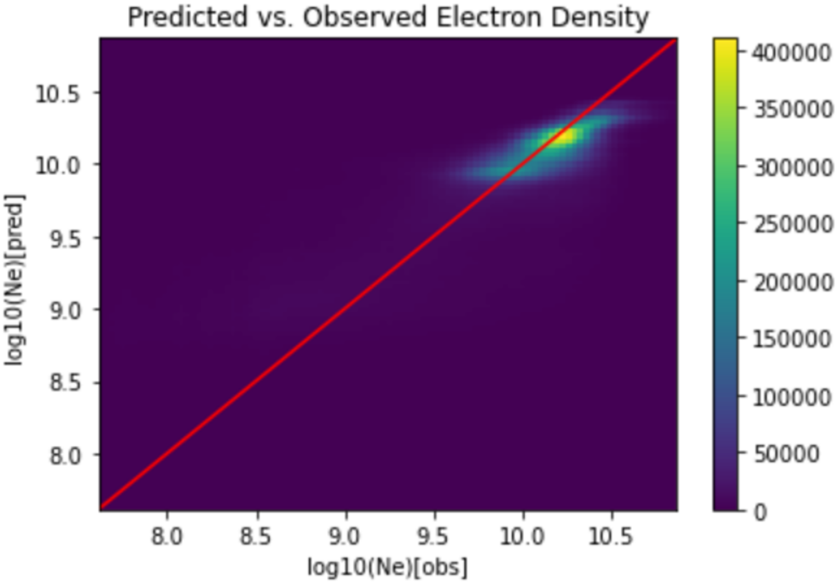

Figure 9: The correlation between the observed electron density and the model's predication of the electron density for the model trained using the DMSP data. The bin size for both the observed and predicted density is equal to 100. The color bar shows the number of observations in each bin. The red diagonal line given by y = x indicates perfect agreement between the model's predictions and observed data.

4.2 Model Application

The magnetospheric model was applied to a geomagnetic storm between March 20th of 2001 and June 10th of 2001 to test the predictive abilities. The eight plots in Figure 10 show the increase in electron density around MLT 18 as a Plasmaspheric plume forms in response to the increased geomagnetic activity of the storm. The top four plots show the electron density plotted as a function of L shell and MLT for four different time steps in 2001: March 20th at 13:59 UT, May 8th at 18:24 UT, May 28th at 22:17 UT, and June 10th at 6:33 UT. The bottom four plots show the same event at the same time steps with the coordinates MLT and L-shell translated to polar coordinates according to the following equation in order to represent a more familiar view of the Earth with the plasmasphere surrounding it:

$$x = L\,sin(MLT - 12) \cdot 15\frac{\pi}{180}$$

$$y = L\,cos(MLT - 12) \cdot 15\frac{\pi}{180}$$

Thus, in this view the L shell increases radially outward, and MLT is a function of the angle around Earth, so that the plots show a horizontal cross-section from above Earth with the nightside of Earth represented by the black side of the circle and the dayside represented by the white side of the circle. When compared to the observed electron densities during this storm event, it is found that successful reconstruction of the expected Plasmaspheric dynamics is achieved. In other words, plume formation is observed along with the expected dates and at the expected coordinates of L shell and MLT. This further demonstrates the model’s accurate predictive abilities. The plots show an increase in electron density as the plasmaspheric plume forms due to the geomagnetic storm.

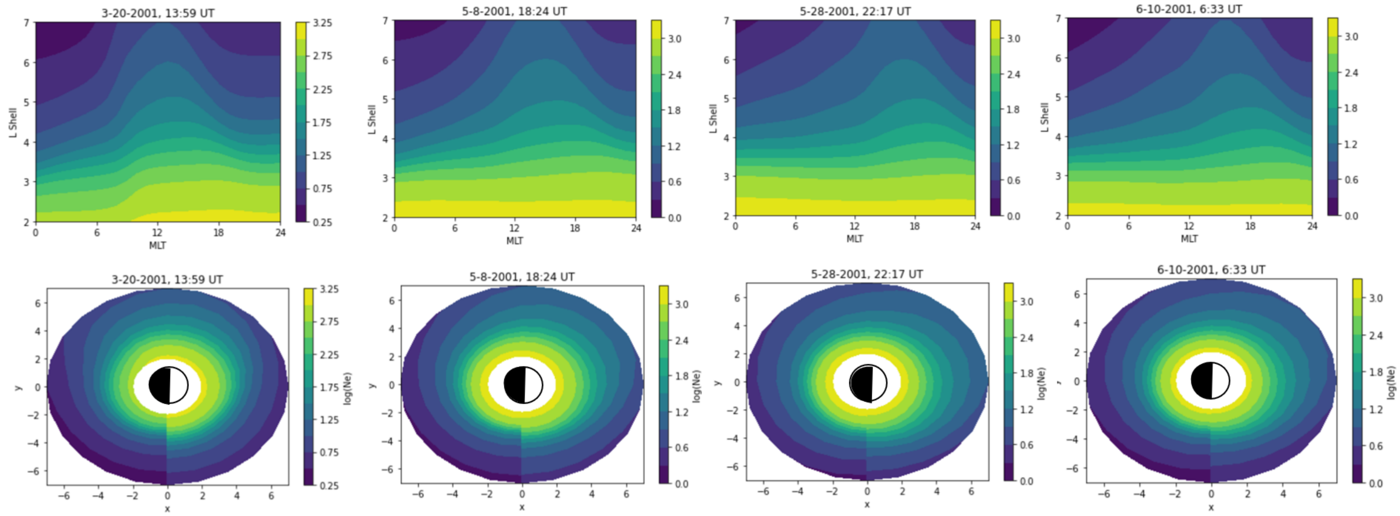

Figure 10: Two-dimensional histogram plots of the logarithm of the electron density as a function of L shell and MLT for four different time steps during a geomagnetic storm event. In the top four plots, L shell is shown on the y-axis and MLT is shown on the x-axis. The bottom four plots show the same data over the same time steps with the coordinates translated to polar coordinates to show a more familiar view, with the L shell increasing radially outward from the center and MLT as an angle around the origin. The center of the bottom plots show the Earth, with the dayside represented by the white half of the circle and the night side represented by the black side of the circle. For each of the four time steps, the plasma density was successfully reconstructed in accordance with what was observed.

At the time of writing this thesis the ionospheric model trained using DMSP data was not able to be applied in order to create useful reconstructions of the electron density. The initial attempt to plot the electron density onto a virtual grid of MLAT and MLT was unsuccessful due to the large spatial areas which the satellite did not cover. The lack of electron density data in these regions resulted in reconstructions that did not accurately reflect the plasma density evolution. Plots can be made that show instead the electron densities over the trajectories of the DMSP satellites over time, but at the time of writing, this was not successfully completed.

Discussion

A time and history-dependent plasma density model of the inner magnetosphere is necessary to understand the energetic particle scattering and the wave excitation and propagation which is influenced by electron density. Previous empirical modes have been limited in their predictive abilities because of their lack of temporal and geomagnetic-activity dependence. In this project, we develop a history-dependent plasma density model using a three-dimensional dynamic electron density model based on an artificial neural network. Two models were developed, one magnetospheric model generated using electron densities from the satellite missions of CRRES, ISEE, IMAGE, and POLAR, and the ionospheric model generated using electron densities from the DMSP satellite missions. Time series of various geomagnetic and solar indices were also used, using data from NASA's OMNI database, resulting in the history dependence of the model. Therefore, the modeled plasma density depends on the preceding state, and produces a spatially and temporally continuous output rather than stepwise.

The magnetospheric model trained using CRRE, ISEE, IMAGE, and POLAR data reproduces plasmaspheric dynamics with an error within a factor of 3, while the model trained using DMSP data reproduces plasmaspheric dynamics with an error with a factor of 5. Overall, the models' predictions showed excellent agreement with electron density observations. There are some limitations in the model's accuracy due to the noise over observations of the instrument measurements. For example, in the magnetospheric model, an error factor of 2.57 was found. However, the noise due to the instrumentation has an error factor of 2, representing a significant portion of that error [*Chu et al.,* 2017a]. The size of the data also presented a limitation due to the finite computing power. The DMSP data, for example, was so large that only a small portion of the data could be randomly selected for use in the model's training process in order to avoid using enormous quantities of computational time.

The magnetospheric model's predictive ability was further confirmed by its successful reconstruction of the plasmasphere's response to a geomagnetic storm event commencing on

March 20th of 2001. The model successfully reconstructed dynamic density features such as the plume formation in response to increased geomagnetic activity.

One of the most important applications of the DEN3D model is the ability to construct time-dependent three-dimensional electron density distributions over time periods for which spacecraft observations are sparse or non-present. The DEN3D model has the ability to convert sparse observations over long periods of time into dense reconstructions for any given instant in time. The reconstruction can then be used to examine potentially important physics which is absent from physics-based models by comparing the modeled values to the physics-based model output. For example, in a study by *Chu et al.,* [2107b] DEN3D was used to calculate the field-aligned density profiles in the noon-midnight meridian for a moderate storm that occurred on June 1st of 2013. In that study, it was found that plasmaspheric depletion during the storm was consistent with storm effects indicated by the SYM-H index, while short-term variation in the plasmaspheric density was modulated by the AL index as well [*Chu et al.,* 2017]. One possible explanation for this effect is magnetospheric processes such as substorm injections, subauroral polarization streams, or enhanced convection influencing plasmaspheric dynamics [*Goldstein et al.,* 2003].

The model can also be applied to study plasmaspheric refilling dynamics. Past determinations of refilling rates have been based off of observation from successive orbits of satellites during storms. The limited data resulted in refilling rates which were assumed to be constant over a few days according to equations for L shell. The refilling was thought to occur at monotonically increasing rates moving in towards earth [*Denton et al.,* 2012; *Krall et al.,* 2016]. Using the DEN3D model, it is found that density variations are not uniform during the storm recovery phase, instead following complex dynamics. The refilling rate depends on both SYM-H and AL indices rather than being constant values during storms. The speed of density depletion and subsequent refilling also depends on the strength of the geomagnetic activity triggering it [*Chu et al.,* 2017a]

A three-dimensional neural network model of the plasmasphere is essential in the study of space weather. The next step in improving these models would be to combine the observations from CRRES, IMAGE, ISEE, POLAR, and DMSP satellites to have a larger database for training and to have data at a larger number of spatial coordinates, thus improving the model's accuracy.

References

A.J. Dessler, J.A. Fejer (1963), Interpretation of Kp index and M-region geomagnetic storms, *Planetary and Space Science, Volume 11, Issue 5,* ISSN 0032-0633, https://doi.org/10.1016/0032-0633(63)90074-6.

Anderson, R. R., D. A. Gurnett, and D. L. Odem (1992), CRRES plasma wave experiment, J. Spacecr. Rockets, 29(4), 570–573, doi:10.2514/

Bortnik, J., W. Li, R. M. Thorne, and V. Angelopoulos (2016), A unified approach to inner magnetospheric state prediction, J. Geophys. Res. Space Physics, 121, 2423–2430, doi:10.1002/2015JA021733.

Cai, L., Ma, S., Cai, H. *et al.* Prediction of SYM-H index by NARX neural network from IMF and solar wind data. *Sci. China Ser. E-Technol. Sci.* **52,** 2877–2885 (2009). https://doi.org/10.1007/s11431-009-0296-9

Carpenter, D. L. (1966), Whistler studies of the plasmapause in the magnetosphere: 1. Temporal variations in the position of the knee and some evidence on plasma motions near the knee, J. Geophys. Res., 71(3), 693–709, doi:10.1029/JZ071i003p00693.

Denton, R. E., J. Goldstein, and J. D. Menietti (2002a), Field line dependence of magnetospheric electron density, Geophys. Res. Lett., 29(24),
2205, doi:10.1029/2002GL015963.

Denton, R. E., J. Goldstein, J. D. Menietti, and S. L. Young (2002b), Magnetospheric electron density model inferred from polar plasma wave
data, J. Geophys. Res., 107(A11), 1386, doi:10.1029/2001JA009136.

Denton, R. E., J. D. Menietti, J. Goldstein, S. L. Young, and R. R. Anderson (2004), Electron density in the magnetosphere, J. Geophys. Res., 109,
A09215, doi:10.1029/2003JA010245.

Denton, R. E., K. Takahashi, I. A. Galkin, P. A. Nsumei, X. Huang, B. W. Reinisch, R. R. Anderson, M. K. Sleeper, and W. J. Hughes (2006), Distribution of density along magnetospheric field lines, J. Geophys. Res., 111, A04213, doi:10.1029/2005JA011414.

Center, National Geophysical Data. "Indices of Magnetic Activity: NCEI." *Indices of Magnetic Activity | NCEI*, U.S. Department of Commerce, 5 Apr. 2010, www.ngdc.noaa.gov/stp/geomag/indices.html.

Chu, X. N., J. Bortnik, W. Li, Q. Ma, V. Angelopoulos, and R. M. Thorne (2017), Erosion and refilling of the plasmasphere during a geomagnetic storm modeled by a neural network, J. Geophys. Res. Space Physics, 122, 7118–7129, doi:10.1002/2017JA023948.

Chu, X., et al. (2017), A neural network model of three-dimensional dynamic electron density in the inner magnetosphere, J. Geophys. Res. Space Physics, 122, 9183–9197, doi:10.1002/ 2017JA024464.

Darrouzet, F., J. De Keyser, P. M. E. Décréau, F. El Lemdani-Mazouz, and X. Vallières (2008), Statistical analysis of plasmaspheric plumes with Cluster/WHISPER observations, Ann. Geophys., 26(8), 2403–2417, doi:10.5194/angeo-26-2403-2008

Darrouzet, F., J. de Keyser, and V. Pierrard (2009), The Earth's Plasmasphere: A CLUSTER and IMAGE Perspective, Springer Science & Business Media, Springer, New York.

Foster, J. C., P. J. Erickson, A. J. Coster, S. Thaller, J. Tao, J. R. Wygant, and J. W. Bonnell (2014), Storm time observations of plasmasphere erosion flux in the magnetosphere and ionosphere, Geophys. Res. Lett., 41, 762–768, doi:10.1002/2013GL059124

Fu, H. S., Tu, J., Cao, J. B., Song, P., Reinisch, B. W., Gallagher, D. L., and Yang, B. (2010), IMAGE and DMSP observations of a density trough inside the plasmasphere, *J. Geophys. Res.*, 115, A07227, doi:10.1029/2009JA015104.

Gallagher, D. L., P. D. Craven, and R. H. Comfort (2000), Global core plasma model, J. Geophys. Res., 105(A8), 18,819–18,833, doi:10.1029/
1999JA000241.

Goldstein, J., B. R. Sandel, M. F. Thomsen, M. Spasojević, and P. H. Reiff (2004), Simultaneous remote sensing and in situ observations of plasmaspheric drainage plumes, J. Geophys. Res., 109, A03202, doi:10.1029/2003JA010281

Goldstein, J. A. Redfern, and B. W. Reinisch (2012), Magnetospheric electron density long-term (>1 day) refilling rates inferred from passive radio emissions measured by IMAGE RPI during geomagnetically quiet times, J. Geophys. Res., 117, A03221, doi:10.1029/2011JA017274.

Grebowsky, J. M. (1970), Model study of plasmapause motion, J. Geophys. Res., 75(22), 4329–4333, doi:10.1029/JA075i022p04329.

Gurnett, D. A., et al. (1995), The Polar plasma wave instrument, Space Sci. Rev., 71(1), 597–622, doi:10.1007/bf00751343.

Huang, X., B. W. Reinisch, P. Song, J. L. Green, and D. L. Gallagher (2004), Developing an empirical density model of the plasmasphere using IMAGE/RPI observations, Adv. Space Res., 33(6), 829–832, doi:10.1016/j.asr.2003.07.007.

John Towns, Timothy Cockerill, Maytal Dahan, Ian Foster, Kelly Gaither, Andrew Grimshaw, Victor Hazlewood, Scott Lathrop, Dave Lifka, Gregory D. Peterson, Ralph Roskies, J. Ray Scott, Nancy Wilkins-Diehr, "XSEDE: Accelerating Scientific Discovery", Computing in Science & Engineering, vol.16, no. 5, pp. 62-74, Sept.-Oct. 2014, doi:10.1109/MCSE.2014.80

Kamide, Y., and Rostoker, G. (2004), What is the physical meaning of the AE index?, *Eos Trans. AGU*, 85(19), 188– 192, doi:10.1029/2004EO190010.

Kersley, L., and J. A. Klobuchar (1980), Storm associated protonospheric depletion and recovery, Planet. Space Sci., 28(5), 453–458, doi:10.1016/0032-0633(80)90026-4.

Kivelson, Margaret Galland, and Christopher T. Russell. Introduction to Space Physics. Cambridge University Press, 1995.

Laundal, K. M., and A. D. Richmond. “Magnetic Coordinate Systems.” *Space Science Reviews*, vol. 206, no. 1-4, 2016, pp. 27–59., doi:10.1007/s11214-016-0275-y.

Lemaire, J., K. Gringauz, V. Bassolo, and D. Carpenter (1998), The Earth’s Plasmasphere, Cambridge Univ. Press, Cambridge, U. K., and New York.

Li, W., Zhao, D., He, C., Shen, Y., Hu, A., & Zhang, K. (2021). Application of a multi-layer artificial neural network in a 3-D global electron density model using the long-term observations of COSMIC, Fengyun-3C, and Digisonde. Space Weather, 19, e2020SW002605. https://doi.org/10.1029/2020SW002605

Li, W., R. M. Thorne, J. Bortnik, Y. Nishimura, V. Angelopoulos, L. Chen, J. P. McFadden, and J. W. Bonnell (2010), Global distributions of suprathermal electrons observed on THEMIS and potential mechanisms for access into the plasmasphere, J. Geophys. Res., 115, A00J10, doi:10.1029/2010JA015687

Machol, J., Snow, M., Woodraska, D., Woods, T., Viereck, R., & Coddington, O. (2019). An improved lyman-alpha composite. Earth and Space Science, https://doi.org/10.1029/ MACHOL ET AL. 2019EA000648

Nishida, A. (1966), Formation of plasmapause, or magnetospheric plasma knee, by the combined action of magnetospheric convection and plasma escape from the tail, J. Geophys. Res., 71(23), 5669–5679, doi:10.1029/JZ071i023p05669.

Ober, D. M., J. L. Horwitz, M. F. Thomsen, R. C. Elphic, D. J. McComas, R. D. Belian, and M. B. Moldwin (1997), Premidnight plasmaspheric “plumes”, J. Geophys. Res., 102(A6), 11,325–11,334, doi:10.1029/97JA00562

Ozhogin, P., J. Tu, P. Song, and B. W. Reinisch (2012), Field-aligned distribution of the plasmaspheric electron density: An empirical model derived from the IMAGE RPI measurements, J. Geophys. Res., 117, A06225, doi:10.1029/2011JA017330.

Reinisch, B. W., M. B. Moldwin, R. E. Denton, D. L. Gallagher, H. Matsui, V. Pierrard, and J. N. Tu (2009), Augmented empirical models of plasmaspheric density and electric field using IMAGE and CLUSTER data, Space Sci. Rev., 145(1–2), 231–261, doi:10.1007/s11214-008-9481-6.

Sandel, B. R., and M. H. Denton (2007), Global view of refilling of the plasmasphere, Geophys. Res. Lett., 34, L17102, doi:10.1029/2007GL030669.

Sheeley, B. W., M. B. Moldwin, H. K. Rassoul, and R. R. Anderson (2001), An empirical plasmasphere and trough density model: CRRES observations, J. Geophys. Res., 106(A11), 25,631–25,641, doi:10.1029/2000JA000286.

Tapping, K.F., Charrois, D.P. Limits to the accuracy of the 10.7 cm flux. *Sol Phys* **150,** 305–315 (1994). https://doi.org/10.1007/BF00712892

Thorne, R. M., et al. (2013), Rapid local acceleration of relativistic radiation-belt electrons by magnetospheric chorus, Nature, 504(7480), 411–414, doi:10.1038/nature12889.

Troshichev, O., Janzhura, A., and Stauning, P. (2006), Unified PCN and PCS indices: Method of calculation, physical sense, and dependence on the IMF azimuthal and northward components, *J. Geophys. Res.*, 111, A05208, doi:10.1029/2005JA011402.

Tu, J. N., P. Song, B. W. Reinisch, J. L. Green, and X. Q. Huang (2006), Empirical specification of field-aligned plasma density profiles for plasmasphere refilling, J. Geophys. Res., 111, A06216, doi:10.1029/2005JA011582.

Wanliss, J. A., and Showalter, K. M. (2006), High-resolution global storm index: *Dst* versus SYM-H, *J. Geophys. Res.*, 111, A02202, doi:10.1029/2005JA011034.